ENGINEERING

Bioinspired wettability boundary stabilizes water sloshing

Jie Ma[1,2], Zidong Zhan[1,2], Zihao Zhang[1,2], Zhuoxing Liu[1,2], Jia Peng[1,2], Cunlong Yu[1,2,3]*, Lei Jiang[1,2,3], Lei Wu[3,4]*, Zhichao Dong[1,2,3]*

Liquid sloshing leads to spillage, waste, and operational inefficiency across multiple industries. Although strategies such as baffle designs and foam inserts exist, they often fall short in real-world dynamic conditions. Inspired by liquid-stabilizing mechanisms of pitcher plants and impact-dampening notches of water lilies, we introduce a dual-biomimetic cup design that enhances liquid stabilization using three-dimensional printing to construct structures and superhydrophobic coating for wettability boundary modification. Our system integrates patterned hydrophilic-superhydrophobic boundaries with strategically placed superhydrophobic notches, synergistically stabilizing water surfaces and dissipating oscillatory energy. Comprehensive tests—including centrifugal, vibrational, and real-world transport scenarios—demonstrated a spill rate of approaching 0%, as well as robust resistance to water sloshing. Notably, a four-tier tower of dual-biomimetic cups mounted on a car retained nearly 100% of their liquid after traversing 50 alternating speed bumps, whereas conventional cups lost more than 40%. Our bioinspired method demonstrates a scalable and versatile approach that bridges natural wetting strategies with practical engineering applications in liquid transport and containment.

INTRODUCTION

Liquid sloshing refers to the free liquid surface motion caused by changes in the acceleration of its container. This phenomenon often leads to contact line movement and even spillage, posing challenges in daily life, industrial operations, and laboratory safety. In detail, ~12% of drinking water loss in households (*1*) creates a slippery surface (*2*) that markedly increases safety hazards (*3*). Individuals with motor impairments, such as patients with Parkinson's disease (*4*, *5*), are particularly vulnerable. Besides daily life problems, liquid sloshing is a challenge in industrial applications (*6*, *7*). For example, during liquid transfer along production lines, cups or tanks often experience sudden accelerations or abrupt changes in direction (*8*), which compromise liquid stability (*9*) and increase the risk of spills (*10*, *11*), leading to operational inefficiencies and product loss due to sloshing. Existing mitigation strategies, including flexible cups (*6*), foam inserts (*9*), slot-baffle systems (*10*), and modified carrying methods (*11*), overlook the role of surface wettability in fluid control, resulting in overly complicated designs but have limited effectiveness in dynamic environments. Over a century ago, Worthington and Cole (*12*) recognized that surface properties of solids affect splashing behaviors, foreshadowing the importance of wettability modulation explored here.

Biomimetics, by emulating structures and mechanisms in nature, offers innovative design strategies for advanced material fabrication (*13*–*16*) and superior liquid handling strategies. These natural strategies include fungal ballistospore discharge (*17*, *18*), desert beetle water capture (*19*), spider silk fog harvesting (*20*), and bombardier beetle fluid propulsion (*21*), all of which use surface wettability and microstructures for effective control. Particularly relevant examples include pitcher plants, which manipulate slippery fluid films spreading on the peristome surfaces (*22*–*24*), and water lilies, which mitigate the impact of water flow via distinctive notches (*25*). These biological exemplars (*26*–*28*) suggest that integrating surface energy modulation and strategic structural features can provide sloshing control.

Here, we demonstrate a dual-bioinspired approach to stabilize water sloshing that integrates two natural principles: the wettability, hydrophilic-superhydrophobic (HL-SHB), boundary inspired by the *Nepenthes* pitcher, which stabilizes the contact line of the water surface on the boundary, and the notched structures inspired by water lilies, which dissipate vibrational energy and resist liquid ascent. Using continuous three-dimensional (3D) printing, we fabricated these containers by sequentially combining HL resins and SHB resins alternatively, achieving a fine balance of macro- and microfeatures for liquid stabilization. We conducted a suite of experiments to rigorously test the dual-biomimetic design, including controlled centrifugal and vibrational experiments that quantified sloshing thresholds. In situ x-ray tomography elucidated the real-time behavior of water sloshing and the pinning effect of the biomimetic features. Furthermore, we tested the dual-biomimetic cups mounted on a compact-sized car navigating 50 alternating speed bumps at 10 km hour^{-1}, a famous vehicle stability test, "champagne tower" challenge, performed by an executive limousine. All four layers of the dual-biomimetic tower retained almost 100% of their liquid contents, contrasting with more than 40% loss in conventional cups. Moreover, we demonstrated robust performance across daily scenarios (walking, cycling, driving, rail travel, and airplane turbulence flying), showing a true leap from laboratory proof of concept to practical, field-ready applications.

RESULTS

Natural boundary stabilizes water surface

Nepenthes, a carnivorous plant thriving in windy tropical rainforests (*29*), is characterized by its pitcher-shaped trap filled with digestive fluids. Stabilizing these digestive fluids without spillage during the shaking by winds in the tropical rainforest climate is crucial for their

[1]Laboratory of Bio-Inspired Smart Interface Science, Technical Institute of Physics and Chemistry, Chinese Academy of Sciences, Beijing 100190, China. [2]School of Future Technology, University of Chinese Academy of Sciences, Beijing 100049, China. [3]State Key Laboratory of Bioinspired Interfacial Materials Science, Suzhou Institute for Advanced Research, University of Science and Technology of China, Suzhou, Jiangsu 215123, China. [4]Key Laboratory of Green Printing, Beijing National Laboratory for Molecular Sciences (BNLMS), Institute of Chemistry, Chinese Academy of Sciences, Beijing 100190, China.
*Corresponding author. Email: yucunlong@mail.ipc.ac.cn (C.Y.); wulei1989@iccas.ac.cn (L.W.); dongzhichao@mail.ipc.ac.cn (Z.D.)

survival (*30*). It has been proposed that an apparent boundary between the upper waxy zone and the lower digestive zone (*31*) exists along the inner wall of the pitcher.

To demonstrate the role of the boundary, we first conducted wettability analysis of the inner wall of *Nepenthes* × *miranda* as a representative, which revealed two distinct regions (Fig. 1A): the digestive zone showing HL with water contact angles of ~49.1° and the waxy zone showing SHB with water contact angles of ~150.2°. These two wettability regions are separated by a sharp wettability boundary with a width of less than 1 mm (Fig. 1B). Lateral adhesive force $F_{\mathrm{lateral}} = \gamma w \Delta\cos\theta$ (*32*, *33*), is measured to characterize the HL-SHB wettability boundary for pining droplet motion, where γ is the water surface tension, *w* is the water droplet width, and Δcosθ is the contact angle hysteresis and $\Delta\cos\theta = \cos\theta_{\mathrm{rec}} - \cos\theta_{\mathrm{adv}}$ with $\cos\theta_{\mathrm{rec}}$ the receding contact angle on the HL side and $\cos\theta_{\mathrm{adv}}$ the advancing contact angle on the SHB side. The *w* and Δcosθ are varied under the dynamic conditions. When a 10-μl water droplet's advancing contact line encounters and crosses the boundary from the digestive zone to the waxy zone, the lateral adhesive force experiences a pronounced increase to a value of 1.8 times the gravitational force of the water droplet (Fig. 1C). This HL-SHB boundary is therefore hypothesized to play a role in stabilizing water sloshing.

Next, we examined 18 additional pitcher plant species, with a total sample size of $N = 72$ (Fig. 1D), including species found and measured in natural habitats, such as *Nepenthes bongso* and *Nepenthes gymnamphora* from Mount Kunyit and *Nepenthes singalana* from Mount Kerinci, Jambi, Indonesia (Fig. 1E, triangle symbols in Fig. 1D, and fig. S1) and *Nepenthes mindanaoensis* and *Nepenthes graciliflora* from the Philippines (Fig. 1E, square symbols in Fig. 1D, and fig. S1). We also included commonly discussed species (*23*, *29*–*31*, *34*–*36*) cultivated in the greenhouse of our laboratory (figs. S2 and S3A), such as *Nepenthes alta, Nepenthes mirabilis*, and *Nepenthes gracilis* (circular symbols in Fig. 1D). We used a portable 3D contact angle machine, KRÜSS Ayríís, and measured the contact angle at *n* different points on the pitcher's inner surface for each pitcher plant (sample size *N*). The measurements generated a dataset expressed as a sample set of size $N \times n$ (Fig. 1D, right), reflecting the water contact angles in the digestive zone and the waxy zone of each species individually by two normal distribution curves (Fig. 1F). The summarizing information was shown in table S1. In particular, the waxy zone curves typically show a narrower spread at the contact angle of ~150.6° (the average value from sample size of $\Sigma(N \times n) = 252$; vertical dashed line in Fig. 1F), indicating more consistent superhydrophobicity in this region, whereas the digestive zone curves are broader, suggesting variability in the HL properties. The range of contact angles observed across these zones highlights the pronounced difference in wettability, confirming the universality of the HL-SHB wettability transition boundary in *Nepenthes* (Fig. 1F).

During field observations on Mount Kunyit and Kerinci in Sumatra, Indonesia, we found that the level of digestive fluid in natural pitchers usually lies at or just below the HL-SHB transition boundary (Fig. 1E and fig. S1). To further explore the role of this boundary in stabilizing fluids, we simulated natural wind conditions and used cultivated pitcher plants in a wind tunnel (fig. S3B and movie S1). We compared three water levels within pitchers: near the boundary, far above it, and far below it (Fig. 1G, left). At a wind speed of ~6 m s^{-1}, we monitored the real-time water height (h_{water}), with minor fluctuations indicating better stability (Fig. 1G, right). Our results lastly showed that the liquid level positioned near the HL-SHB boundary exhibited markedly greater stability compared to levels far above (where spillage occurred) or far below (where sloshing occurred with more obvious fluctuations) the boundary (Fig. 1G, right). In addition, we conducted centrifugal (lateral acceleration; fig. S4) and vertical vibration (vertical acceleration; fig. S5) experiments (detailed parameters shown in Materials and Methods) to examine the sloshing behavior and found that the HL-SHB boundary enhanced water surface stability by minimizing disruptive sloshing. These results collectively support the role of the HL-SHB boundary in enhancing water stability within the pitcher under windy conditions.

Redesigning nature's boundary for engineering

To demonstrate the practical ability of the wettability boundary in stabilizing sloshing, we examined and summarized the typical types and magnitudes of accelerations encountered in real-world scenarios. Measurements simulating various transportation modes (cars, trains, and airplanes) and human activities (walking and cycling) showed that vertical acceleration changes (Δa_z) are larger than the lateral ones (Δa_x), and they both generally remain within 1.0*g* (Fig. 2A and Materials and Methods). Extreme lateral accelerations can reach up to 1.4*g* in high-performance vehicles (*37*), while more moderate values ranging from 0.1 to 0.4*g* (Fig. 2A) occur during high-speed train departures (*38*) and airplane takeoffs (*39*).

To systematically replicate the lateral dynamic forces, we developed a rotational platform (Fig. 2B) capable of imposing controlled centrifugal accelerations up to 11.0*g* (movie S2). The apparatus consisted of a motorized rotor with a 2.0-m-diameter arm (Fig. 2B and fig. S4A). Two sample holders were mounted at either end of the arm, each equipped with synchronized high-speed cameras and adjustable lighting to enable precise observation under identical conditions (Fig. 2C). By controlling the rotational speed of the arm, centrifugal accelerations were generated according to $a_{\omega} = \omega^2/R$ (*40*), where ω was the angular velocity and *R* was the radial distance from the samples to the rotation center.

Models for sloshing stability measurements included both 2D plates and 3D cups with different wettability or distributions, all fabricated via 3D printing (Materials and Methods). Centrifugal and vertical vibration experiments were systematically conducted to replicate practical conditions, with the initial water height set precisely at the HL-SHB boundary. For comparison, control models were also constructed, including both 2D plates and 3D cups with homogeneous wettability (either entirely HL or entirely SHB).

First, we evaluated the behavior of water droplets deposited on 2D plates with uniform HL surface and horizontally patterned plates with HL-SHB boundary (Fig. 2C). The HL resin shows a contact angle of 37.6° ± 1.6° and a vertical drop-solid adhesion force of 222.3 μN, and the SHB one shows 166.1° ± 2.5° and 15.9 μN (fig. S6). By tracking the droplet displacement (*x*) under increasing centrifugal acceleration (a_{ω}/g) in Fig. 2D, we found that droplets on uniformly HL surfaces slide freely once the acceleration exceeds ~2.0*g*. In contrast, the droplet was pinned at HL-SHB boundaries even under acceleration up to ~3.5*g*, which is 1.75 times that of a uniformly HL surface (Fig. 2D and fig. S7). This enhanced stability is attributable to an increase in contact angle hysteresis ($\Delta\cos\theta = \cos\theta_{\mathrm{rec}} - \cos\theta_{\mathrm{adv}}$) (*41*, *42*) and an expansion in droplet contact width (*w*) at the HL-SHB boundary (fig. S7). Both of these factors amplify the droplet critical acceleration, $a_{\mathrm{c-drop}} = \frac{\gamma w}{m}\Delta\cos\theta$, in the critical state, when the three-phase contact line will cross the boundary but has not yet crossed into the

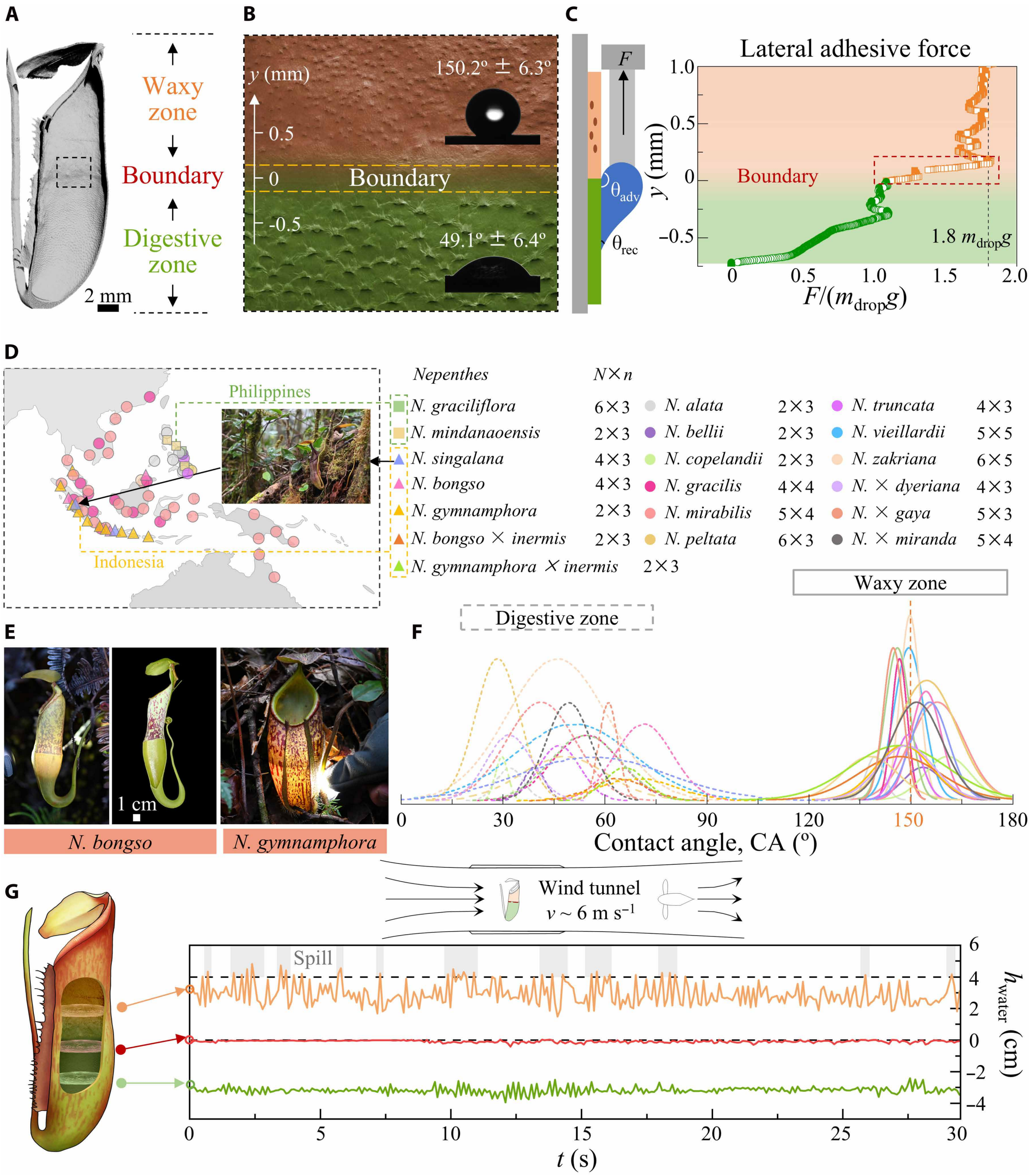

Fig. 1. Pitcher with a wettability boundary stabilizes water sloshing. (**A**) Micro-CT image of *Nepenthes* × *miranda* reveals an upper waxy zone and a lower digestive zone. (**B**) Scanning electron microscope (SEM) image and contact angle (CA) measurement of the inner wall of the pitcher at the boundary of the digestive and waxy zones. (**C**) Comparison of water droplet adhesion forces along the inner wall of the pitcher, from the digestive zone to the waxy zone, and crossing the boundary. (**D**) Distribution maps of 19 species of *Nepenthes*, where triangles represent natural *Nepenthes* found on the Sumatra island, squares represent natural *Nepenthes* found in the Philippines, and circles represent cultivated *Nepenthes*, respectively. *N* represents the pitcher sample number, and *n* represents the number of tests on each sample surface. (**E**) *Nepenthes bongso* and *Nepenthes gymnamphora* are found on the Sumatra island. (**F**) Mapping of wettability differences across 19 *Nepenthes* species highlights the contrasting properties of the digestive and waxy zones. (**G**) Pitcher is tested under controlled wind tunnel conditions ($v \sim 6$ m s^{-1}). Water is poured into the tank to keep the water surface near the boundary, far above it, and far below it. Temporal variations in the water height (h_{water}) were recorded and analyzed. The light gray means water spill. Photo credit of field *Nepenthes* image in (D) and (E): X. Xie, Chinese Academy of Sciences.

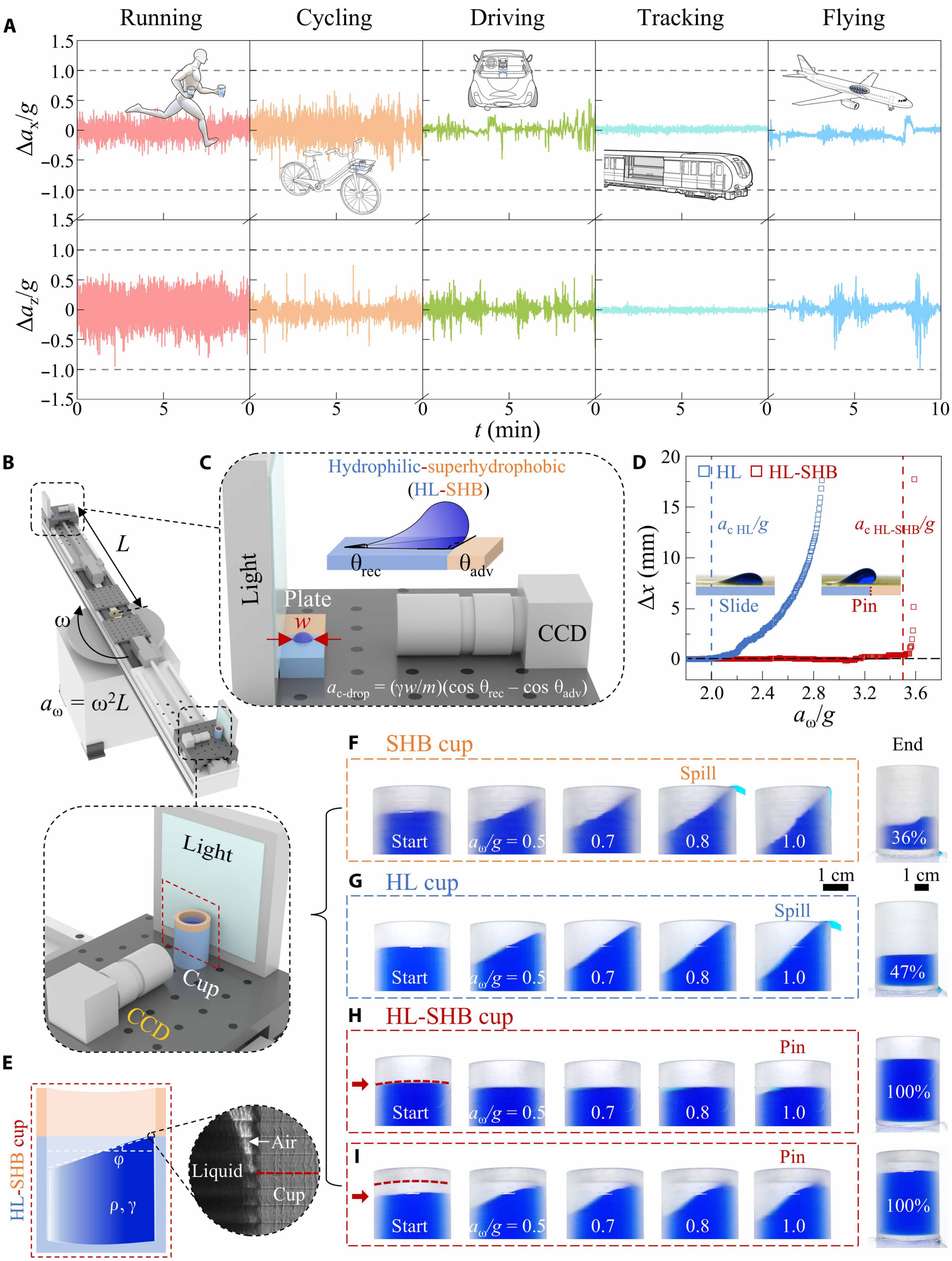

Fig. 2. Wettability boundary stabilizes sloshing. (**A**) Measurements of lateral and vertical accelerations during human activities (walking and cycling) and transportation modes (driving by car, tracking by high-speed train, and flying via airplane). (**B**) Rotational device design. (**C**) Schematic showing a drop approaching the HL-SHB boundary on a plate under rotating conditions. (**D**) Measurement of positions (x) of advancing three-phase contact line versus a_ω/g of drop on an HL or HL-SHB plate. Drop volume is 10 μl. (**E**) Scheme and in situ synchrotron x-ray tomography of the water surface in an HL-SHB cup. White dashed lines indicate water surface variation during rotation, and φ is the water variation angle. Water stable pins at the HL-SHB boundary (red dashed line) and trapped air pockets resist water from further climbing the inner wall. (**F** to **I**) Observations and analyses of liquid sloshing in SHB, HL, and HL-SHB cups demonstrate the effectiveness of the HL-SHB boundary in stabilizing sloshing. Red arrow demonstrates the HL-SHB boundary.

SHB region. The calculated $a_{\text{c-drop}}$ is 2.10g on the HL substrate and 3.57g on the HL-SHB one, which is quantitatively consistent with the experimental values shown in Fig. 2D. The HL-SHB boundary pins the drop even when the $\theta_{\text{incline}} = 90°$ and the F up to $3.1m_{\text{drop}}g$ in vertical direction (fig. S8).

Subsequently, we extended the analysis to biomimetic cups with different wetting distributions on the inner surfaces, including homogeneous SHB, homogeneous HL, and HL-SHB boundary conditions. The biomimetic cup design was inspired by the observation that the diameter ($2R_{\text{pitcher}}$) of the pitcher is approximately 10 times the capillary length (length scaling factor $l_c = (\gamma/\rho g)^{1/2}$, expressed by the liquid density ρ and gravity g, which is typically 2.7 mm for water at 20°C) and is a key geometrical feature summarized from 19 *Nepenthes* species (fig. S9A). For a natural *Nepenthes* pitcher, the HL-SHB boundary is maintained at almost half the height of the pitcher (fig. S9B), leading to dynamic equilibrium for survival. However, for real-world dynamic conditions, the middle location of the HL-SHB boundary is unreasonable for carrying more water. We therefore positioned the HL-SHB boundary in the upper region based on the design principle of allowing for sufficient water storage in the HL region while preventing water overflow from the SHB region.

Under centrifugal lateral forces, the position change of the mass center of sloshing liquid alters the position of the water surface (Fig. 2E). The pressure in the lateral direction, $P = 2R\rho a_\omega$ (*43*), forms the lateral force, and a_ω is the centrifugal acceleration of water inside the cup. The equilibrium moment force along the lateral can be expressed as the shaking part, $F_{\text{shaking}} = \pi R\rho a_\omega \int_0^{2R\tan\varphi} \frac{2R\tan\varphi - \Delta h}{\tan\varphi} d(\Delta h)$, and the relatively static part, $F_{\text{static}} = \pi RhP - 4\pi\rho R^3 a_\omega \tan\varphi$, where h is the undisturbed height of the static water surface, φ is the variation angle, and Δh is the height between the liquid surface and the horizontal plane. The simplified lateral force causes water deformation and rising, $F_{\text{lateral}} = 2\pi R^2 \rho a_\omega (h + R\tan\varphi)$. The cup featuring an HL-SHB boundary exhibits pinned menisci (Fig. 2E, inset) and controls the liquid surface φ with $\tan\varphi = \frac{a_\omega}{g} - \frac{\gamma\Delta\cos\theta}{2R\rho g h}$ (Fig. 2E). Considering the inclined deformation of fluid, the change of liquid position, Δh, can be expressed as

$$\Delta h = \frac{R^2 a_\omega}{6g^2 h}\left(a_\omega - \frac{\gamma\Delta\cos\theta}{R\rho h}\right) \quad (1)$$

which indicates that the liquid change height, Δh, is correlated with the contact angle hysteresis. Specifically, at the same a_ω, the larger $\Delta\cos\theta$ on the cup causes less lateral force and Δh.

The initial liquid height is controlled to the height near the HL-SHB boundary height for all cups. For homogeneous SHB (Fig. 2F) and HL cups (Fig. 2G), if the liquid position, $h + \Delta h$, surpasses the cup's edge, then the liquid will overflow and spill. Moreover, the SHB cup displayed less stabilizing property than the HL cup, which can be due to its hydrophobic nature with a minor $\Delta\cos\theta$ (Fig. 2F). Unlike the continuous ascent observed in homogeneous SHB (Fig. 2F) or HL (Fig. 2G), cups featuring HL-SHB boundaries effectively halt the rise of liquid at the boundary (Fig. 2H) and stabilize water sloshing even when the water surface has a height below the boundary (Fig. 2I). Quantitative measurements of the contained water mass before and after centrifugal acceleration (all from 0.1 to 1.0g for 32.5 s) indicate that HL-SHB boundaries in cups markedly reduce spillage by more than 53% compared to the HL cup and by 64% compared to the SHB one (Fig. 2, F to H). This closely replicates the performance observed in natural *Nepenthes* pitchers (fig. S4B).

Vertical vibration experiments were conducted using a vibration stage to simulate real-world oscillatory motions, such as those encountered during running, cycling, vehicular travel, or flight. The vibration can be described through harmonic excitation (*11*) by the function $Z(t) = A_0\cos(2\pi ft)$, where A_0 is the amplitude (maximum is 5 mm in this work) (Fig. 3A). The corresponding vertical acceleration of liquid film is given by $a_v = -A_0(2\pi f)^2$. Under oscillatory conditions, water was reported to gradually climb and wet the sidewall (*44–46*).

We used a backlit imaging system to assess the performance of cups with different wetting properties. For homogeneous HL, progressive wetting resulted in complete spillage within just 4.5 s (Fig. 3B). With constant vibration energy input, water surfaces experienced a larger Δh and shorter spillage time than those under lateral forces (Figs. 2G and 3B). The water surface positioned nearer the HL-SHB boundary had a smaller Δh compared to surfaces located farther from the boundary. The configuration, with seven-eighths of the inner surface being HL and the remaining one-eighth SHB, was designed to ensure an optimal balance that maintains an adequate water amount (fig. S10) and extends the duration by 120%, allowing the system to withstand up to 100 oscillation cycles without spillage (fig. S11). Although the bioinspired HL-SHB cup performs well during a short oscillation time (in minutes), a gap remains in terms of long-term practical stability.

Structural notch enhancing slosh resistance

Nymphaea water lilies have been demonstrated to have the characteristic notched structure on the leaf edge (*25*) that can maintain exceptional stability in flowing or vigorously vibrated water (Fig. 3C). Inspired by this notch-induced damping stabilizing mechanism, we integrated notches into the SHB part of the HL-SHB cups (Fig. 3D and fig. S12). The incorporation of a notch structure and a 30° notch design can enhance lateral stability compared to the HL-SHB design without a notch (fig. S13). Through systematic optimization, a characterized notch size, one-seventh of the cup diameter, was identified as the optimal cup design parameter (fig. S14) for sufficient energy dissipation. Closely resembling the performance of the natural water lily (*25*), the introduction of arrayed notched structures can maintain over thousands of vibration cycles without spillage in hours (Fig. 3D and movie S2). The formation of a stabilized and Gaussian-curved water surface confined at the HL-SHB notch interface can sufficiently constrain water movement, as confirmed by x-ray synchrotron imaging (Fig. 3D, inset, and fig. S15).

Performance of the dual-biomimetic structure

To evaluate the performance of the dual-biomimetic design, which integrates a *Nepenthes*-inspired HL-SHB boundary with *Nymphaea*-inspired SHB notches, we systematically compared 3D cups with designs involving surface treatments and structural configurations for their ability to suppress water sloshing (Fig. 3E). In detail, homogeneous surfaces (either HL or SHB), single-boundary designs (HL-SHB or SHB-HL from cup bottom to top) are 3D printed as controls. Among all tested configurations, the dual-biomimetic cup exhibited the most effective sloshing resistance (Fig. 3E).

Specifically, introducing notches to a cup with only surface wettability modulation, i.e., homogeneous SHB, SHB (bottom)–HL (top), and HL surfaces, improved the threshold droplet acceleration to 160, 157, and 132%, respectively (Fig. 3E). The critical water

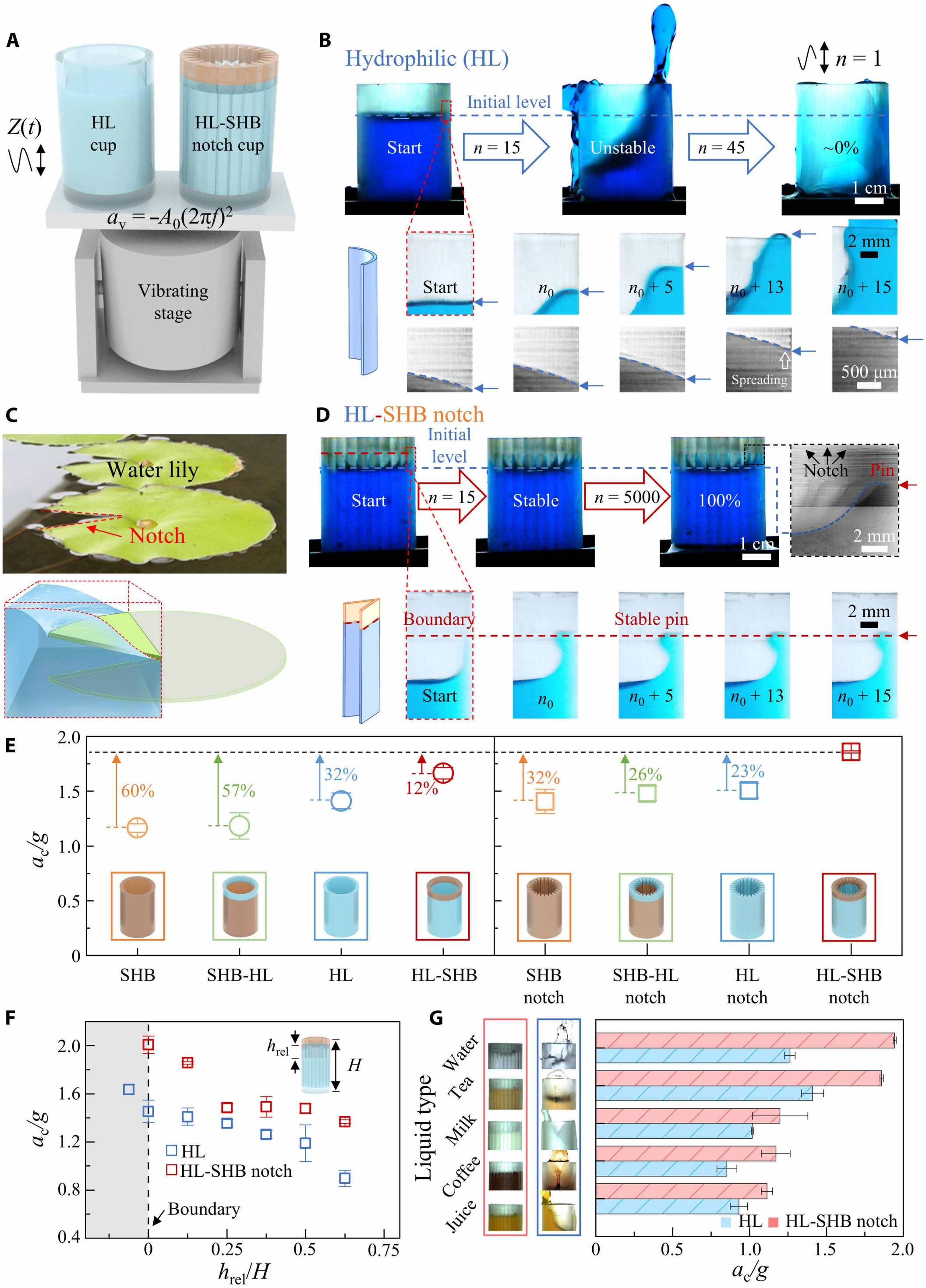

Fig. 3. Structural notch enhancing slosh resistance. (**A**) Vibration setup assesses sloshing in HL and dual-biomimetic cups. (**B**) Water movement in HL cup. First row: Water completely spills from cup after 45 vibrations, lasting just 4.5 s. Second row: Water progressively wets sidewall after 15 vibrations. Third row: In situ x-ray videoing the water ascending dynamics. (**C**) Notch of water lily pins air-water interface and damps water wave impact. (**D**) Optical and x-ray imaging of water surface movement in complete and single-cell HL-SHB notch designs. HL-SHB notch reduces sloshing. (**E**) Measured a_c/g values for cups with various homogeneous HL or SHB surfaces, single-boundary designs (HL-SHB or SHB-HL from cup bottom to top) without notches (left). Introducing notches to cups with surface wettability of homogeneous SHB, SHB (bottom)–HL (top), HL, and HL (bottom)–SHB (top) improves the threshold accelerations (right). (**F**) Relative liquid height (h_{rel}/H) determines a_c/g. Liquid height including liquid below, at, and above (gray background) the HL-SHB boundary. (**G**) Comparison of a_c/g values for HL and dual-biomimetic cups across water, tea, milk, coffee, and juice. Photo credit of water lily in (C): Z.D., Chinese Academy of Sciences.

droplet acceleration, a_c, is governed by the effective radius of the capillary channels within the notch, r_{eff}, and the wettability boundary contrast, $\Delta\cos\theta$, and can be described by the following equation

$$a_c = \frac{\gamma \Delta \cos\theta}{\rho h_{rel}} \left(\frac{1}{R} + \frac{1}{r_{eff}} \right) \quad (2)$$

where ρ is the liquid density, h_{rel} is the liquid height relative to the boundary, and R is the radius of the cup. The synergistic effect of the HL-SHB boundary and the reduced r_{eff} of the notched structure markedly enhanced contact line pinning (fig. S16), effectively preventing upward fluid migration and offering strong resistance to oscillatory disturbances (movie S2).

Adding an SHB-HL boundary to a notched cup further elevated the threshold acceleration by 132% compared to the SHB notch alone, 126% compared to the SHB-HL notch, and 123% relative to the HL notch configurations (Fig. 3E). Compared with other structures (circular, trapezoid, and square), the wedge notch structure inspired by the water lily shows the superior performance in reducing liquid sloshing due to the energy dissipation ability (fig. S17). As observed in the *Nepenthes*, the liquid near the HL-SHB boundary, smaller h_{rel}, is the most stable with a_c even exceeding 2.0g, and once the liquid surpasses the boundary, stability is reduced. The critical liquid height is the location of the boundary, which means the liquid near and below the critical height is stable (Fig. 3F).

The dual-biomimetic cup also demonstrated robust operational versatility. Across a broad range of vibration frequencies (8 to 20 Hz; fig. S18), it consistently maintained a higher critical acceleration than the most severe HL cup, surpassing all conventional and single-feature designs. In the lower lateral frequency (3 Hz), the notched cups also show excellent stability for the liquid transportation (fig. S19). Furthermore, the cups are universal to a variety of everyday liquids, including water, tea, milk, coffee, juice, and carbonated beverages (Fig. 3G and fig. S20). The combined stabilization effects of the HL-SHB boundary and SHB notches markedly raised the threshold acceleration for liquid destabilization, outperforming both traditional and single-biomimetic systems (Fig. 3, E to G).

Real-world dynamic environment testing

To validate its practical utility under real-world dynamic conditions, we retrofitted the dual-biomimetic structure onto disposable paper cups (fig. S21; referred to as the notched paper cup) for testing, with a commercial paper cup serving as a control. Walking stability is first characterized as the typical motion of daily life, as displayed in Fig. 4A and fig. S22. Compared with notched paper cups, commercial paper cups lost more than 30% of their contents within 40 s and more than 50% within 150 s (Fig. 4, B and C), the notched paper cups retained nearly all of their liquid during walking tests (movie S3). Similar results can also be achieved during walking on the treadmill, indicating its liquid-stabilizing capability for daily gentle conditions.

Next, more intense conditions such as walking, cycling, driving, and air travel (including cruising and landing phases involving marked accelerations) are characterized and compared, during with two kinds of cups were mounted on participants' hands, inside bicycle basket, inside a driving vehicle, and a flying aircraft during the whole flight (Fig. 4D and figs. S23 and S24), respectively. Liquid movement was monitored using high-speed imaging, and acceleration data were recorded via integrated sensors (figs. S23A and S24A). Under these conditions, the dual-biomimetic notched cup consistently achieved up to 100% spill prevention, maintaining stability during rapid acceleration, sudden stops, sharp turns, and in-flight turbulence (Fig. 4D and figs. S23B and S24B). High-speed footage confirmed that the HL-SHB boundary effectively pinned the contact line (movie S3). At the same time, the SHB notches dissipated vibrational energy, which is consistent with the mechanism and results of the 3D printed cups. Moreover, the notched cup had no residual, as the HL cup showed after pouring water, simulated by a mechanical arm, demonstrating the usability of the notched cup (fig. S25).

Extreme conditions of a four-tier tower of notched cups (fig. S26) mounting on the vehicle roof, which was driven over a specially arranged test track featuring 50 speed bumps (3 cm in height and 30 cm in width), was conducted to validate the dual-biomimetic design's scalability and real-world applicability (Fig. 4E). To increase the complexity of road conditions further, we alternately positioned these speed bumps under the left and right wheels at 1-m intervals, creating a complex, asymmetric, multidirectional vibration environment over a total distance of 50 m in an internal road. The sport utility vehicle (Haval H6 SUV, Great Wall Motor, China) maintained a constant speed of 10 km hour^{-1} during the test (fig. S27A). The conventional paper cups exhibited marked spillage, where the upper location of the cups resulted in a greater amount of liquid being lost. Notably, the cups in the uppermost layer lost more than 40% of their liquid volume (Fig. 4F and fig. S27B), while all four layers of the dual-biomimetic cup tower retained their liquid contents throughout the entire trial under the same conditions. These findings underscore not only the superior sloshing resistance of the dual-biomimetic cup but also its scalability and robustness under real-world, complex dynamic events involving lateral, vertical, high-amplitude oscillatory conditions.

DISCUSSION

We demonstrated a dual-biomimetic strategy for controlling water sloshing, combining the liquid-trapping boundary inspired by pitcher plants with the impact-dampening notches derived from water lilies. Our approach stabilizes liquid surfaces and dissipates oscillatory energy, achieving up to 100% spill prevention under various dynamic conditions. The implications of these findings extend far beyond laboratory demonstrations. The ability to prevent liquid spillage during sudden maneuvers or while crossing speed bumps could markedly improve the performance and safety of not only beverage cups but also critical systems such as automotive fuel tanks, hydraulic circuits, and cooling systems. This technology offers marked potential in aerospace engineering, where precise fluid control is essential for maintaining system stability during high-speed flight. Similarly, minimizing liquid oscillation in intravenous bags and infusion systems could enhance patient safety and treatment efficiency in medical devices.

MATERIALS AND METHODS

Biological specimens

The optical image and contact angle measurements of natural *Nepenthes* pitcher samples were captured and performed in tropical rainforests on Sumatra island, Indonesia, and Philippines (exact coordinates withheld for conservation reasons) using a Nikon Z6 II camera with a 50-mm lens (Nikon, Japan) and a 3D contact angle instrument (Ayríís, KRÜSS GmbH, Germany). All plant specimens were collected ethically, ensuring minimal environmental impact and adhering to

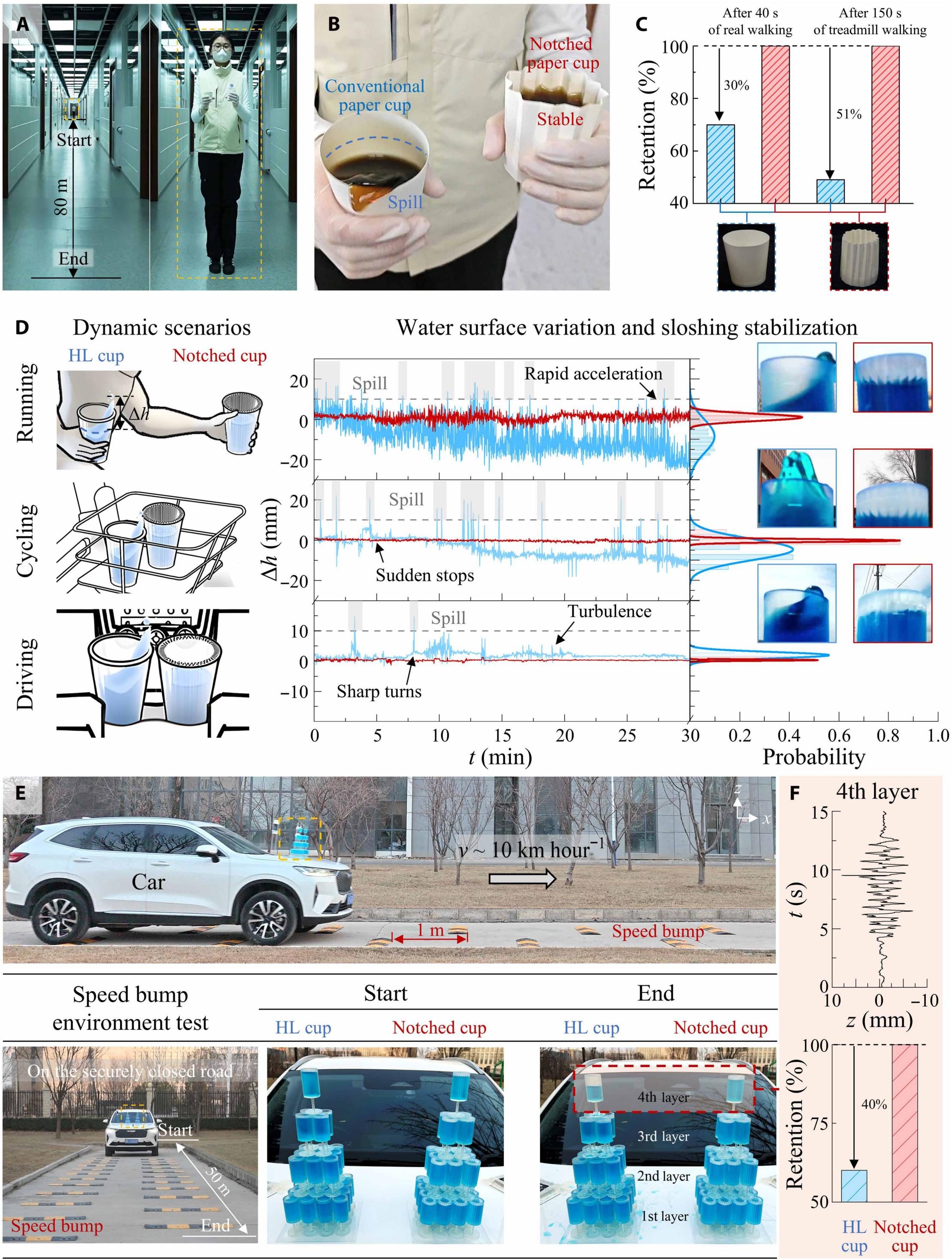

Fig. 4. Comprehensive testing in real-world dynamic environments. (**A**) The user carries both conventional and notched paper cups while walking. (**B**) When walking, water in the commercial paper cup spills, and the notched paper cup remains stable. (**C**) Commercial paper cups lost more than 30% water within 40 s and more than 50% within 150 s, while the notched paper cups lost 0% during walking tests. (**D**) Change in liquid surface height (Δh) in the control and the dual-biomimetic cup during running, cycling, and driving. The light gray means water spill. (**E**) Four-tier tower of HL and notched cups are mounted on the vehicle roof to navigate extreme conditions with alternately positioned speed bumps road in 10 km hour^{-1}. Optical photos of the four-tier tower at the start and end. (**F**) Vibration data for the fourth layer (z) over time (t) during the test (top). The uppermost layer cup (red background) of the HL tower lost 40% water, while the notched cup tower retained water stability and lost 0% under the same conditions (bottom).

local and institutional guidelines. Cultured *Nepenthes* pitcher samples were obtained from the tropical botanical market or botanical garden under proper permits and were grown in a climate-controlled growth chamber at the Technical Institute of Physics and Chemistry, Chinese Academy of Sciences, Beijing, China, at 30°C with 70% relative humidity during the day and 24°C with 90% relative humidity during the night to resemble the conditions of the natural habits and ensure the tropical growth of *Nepenthes*.

Design and fabrication of the dual-biomimetic cup

The dual-biomimetic cup was designed using the 3D Studio Max software (Autodesk, USA) and integrated notches mimicking the peristome ridges of the *Nepenthes* and the notched leaf margins of water lilies. Fabrication was performed via digital light processing (DLP)–based continuous 3D printing using a bottom-up continuous printing strategy on a DLP Pro6500s system (Texas Instruments, USA), with an X-Y resolution of 33 μm and a Z resolution of 10 μm, and the printing and elevating speed is 20 μm s^{-1}.

The HL and SHB regions of the dual-biomimetic cup were fabricated using High Temp V2 resin (Formlabs, USA). The cup was printed using SHB photosensitive resin, followed by a high-temperature HL resin to create the SHB-HL boundary. After printing, parts were soaked in isopropanol (≥99.7%) for 10 min to remove uncured resin. Post-curing was conducted using an ultraviolet chamber equipped with 20 omnidirectional 405-nm light-emitting diodes for 10 min to ensure cross-linking and enhance mechanical integrity.

Wettability and adhesion characterization

Static contact angles were measured using two types of goniometers (DSA25S and Ayriís, KRÜSS GmbH, Germany) using 2-μl deionized water droplets. Dynamic wettability was assessed by recording the sliding angle of 10-μl droplets under controlled tilting using LSA 100 (LAUDA Scientific, Germany).

The surface adhesion force between the water drop and the substrate was quantified via force-distance measurements using a microbalance tensiometer (DCAT11, Dataphysics, Germany), with a motor speed of 0.10 mm s^{-1} and an immersion depth of 2.00 mm. Hanging 10-μl droplets were progressively moved upward from the digestive zone into the waxy zone to evaluate the lateral adhesion on the *Nepenthes* inner wall surfaces.

Microscopy and surface characterization

Scanning electron microscope analysis

Morphological analysis was conducted using an environmental scanning electron microscope (SEM) (Quanta FEG 250, FEI, USA). Before imaging, specimens were fixed on a sample table using conductive copper tape and sputter coated with a 10-nm layer of platinum using an ion sputter coater operated at 10 mA for 60 s.

Micro-CT imaging

Micro-CT imaging was performed on intact *Nepenthes* pitcher samples using a SkyScan 1272 micro-CT scanner (Bruker, USA). Imaging conditions included a 20-kV x-ray source with no filter, a 13.1-μm pixel size, and a rotation step of 0.2° over a full 360° rotation. Data were reconstructed using the NRecon software and analyzed using CTAn and CTVox (Bruker, USA).

Wind tunnel experiment

Wind resistance experiments were conducted in a controlled wind tunnel (HIF-1-(A)-7A, Foshan, China) delivering wind speeds of ~6 m/s, verified with an anemometer (AS-8336, Smart Sensor, Hong Kong, China). The *Nepenthes* pitcher was fixed to a linear translation stage (RXP80, Chengdu Ruixin Technology, China), allowing controlled adjustment relative to the airflow. A high-speed camera (Wave, Freefly Systems, USA) with a 50-mm lens (Nikon, Japan) captured liquid motion at 1000 frames/s (fps). To enhance visual contrast during experiments, deionized water was dyed with brilliant blue food coloring (Aladdin, Shanghai, China) at a concentration of 0.075 g $liter^{-1}$. The surface tension is 70.8 ± 0.1 mN m^{-1}, viscosity is 0.98 ± 0.02 mPa/s, and the density is 999.9 ± 1.1 kg m^{-3} of the dyed solution at 25°C.

Centrifugal stabilization testing

To quantify lateral stability, cups were mounted on a custom centrifuge. Fluid motion was recorded from the rotating frame using a front-facing camera (U3-3060CP-C-HQ Rev.2.2, IDS Imaging, Germany) at 800 by 800 pixels and 100 fps. Fluid was preloaded before the rotational velocity was increased gradually with an angular acceleration of 0.035 rad s^{-2}. The radial distance from the samples to the rotation is 0.95 m, and the angular velocity ranged from 0 to 600° s^{-1}, corresponding to a centrifugal acceleration up to more than 11.0g, calculated by $a_\omega = \omega^2/R$.

Vertical vibration testing

Vertical vibration resistance was evaluated using a shaker system composed of a signal generator (SA-SG030), power amplifier (SA-PA010), and vibration actuator (SA-JZ002). The vibration waveform ($Z(t) = A_0\cos(2\pi ft)$) was tuned by adjusting the generator's output voltage. The vibration stage produced controlled sinusoidal motion with amplitudes ranging from 0 to 5.5 mm and frequencies of 8 to 20 Hz in fig. S16, and others are 10 Hz. The corresponding peak acceleration was calculated using $a_v = -A_0(2\pi f)^2$. Liquid dynamics were imaged using a Nova S9 high-speed camera (Photron, Japan) with a 105-mm macro lens (Nikon) at 1000 fps and a resolution of 1024 by 512 pixels.

In situ synchrotron x-ray microtomography imaging

Real-time internal imaging of water motion during vibration was performed using in situ synchrotron x-ray microtomography at the BL13HB beamline of Shanghai Synchrotron Radiation Facility (SSRF). The beam operated at 16 keV (Super B 2.3T source), and images were captured using a charge-coupled device (CCD) detector at a resolution of 5.5 μm per pixel and 100 fps.

Real-world application testing

Comprehensive real-world experiments were conducted across multiple transport environments. Experiments were conducted under walking, cycling, driving, and flying conditions for a continuous duration of 30 min after arriving at a steady speed and repeated three times per condition at an interval of 20 min. The walking speed is ~5.4 km $hour^{-1}$, the cycling speed is ~12 km $hour^{-1}$, the driving speed is ~45 km $hour^{-1}$, and the flying speed is ~850 km $hour^{-1}$. In the outdoor test, the temperature is 10° to 25°C, and the maximum wind speed is 5 m s^{-1} to avoid the influence of extreme weather on the experiment. Dual-biomimetic and control cups were held by human hands during walking and treadmill running, bicycle handlebars, and car cupholders during urban driving, passenger tables on CR400BF high-speed trains (Shanghai-Beijing route), and seat trays aboard C919 aircraft (Beijing-Shanghai flight). Vehicle types included

Haval H6 (Great Wall Motor, China) and Tesla Model Y (Tesla, USA). A total of 50 speed bumps (3 cm in height, 30 cm in width, and 1.0 m apart) was laid over a 50-m track, with bumps alternating left/right sides. The SUV crossed the course at a controlled speed of 10 km hour^{-1} with a four-tier tower of cups mounted on the engine hood.

Liquid motion was recorded using a DJI Action II camera at 120 fps to assess the liquid stability, and acceleration data were acquired using embedded accelerometers sampling at 100 Hz (Sensor Logger, developed by Kazumasa Wakamori) to evaluate the acceleration. Image-based tracking of triple-phase contact lines and sloshing amplitudes was processed using Tracker 6.1.3 software. All experimental operations strictly followed institutional safety protocols and ethical guidelines, with risk assessments conducted in advance to ensure the safety of personnel, specimens, and equipment.

Lateral transportation was simulated by the displacement axis (57BYG250B, Chengdu Linkage Ruixin Technolog, China) and recorded by the digital camera (Nikon D750, Japan) with a 60-mm macro lens (Laowa) at 50 fps.

Mechanical arm simulation movement

The residues of HL and notched cups were tasted using the mechanical arm (R630, SDCQ, China) by simulating the pouring of water. The residue was calculated by the residual water quality shown by the balance (Shanghai HoChoice Industrial, China).

Theoretical estimation of the rotating condition

Because of the rotation of the water, the surface inclines and can be divided into the relative static part and the relative shaking part. The force of the relative static part can be expressed as $F_{\text{static}} = PA_{\text{static}} = \pi RhP - 4\pi\rho R^3 a_\omega \tan\varphi$, where A_{static} is the static area in the lateral direction, $A_{\text{static}} = \pi Rh_{\text{static}} = \pi R(h - 2R\tan\varphi)$. The force of the relative shaking part can be expressed as $F_{\text{shaking}} = m_{\text{shaking}} a_\omega = \rho V_{\text{shaking}} a_\omega = \pi R\rho a_\omega \int_0^{2R\tan\varphi} \frac{2R\tan\varphi - \Delta h}{\tan\varphi} d(\Delta h)$

Considering the shape change of the rotating water, the change of the center of the water gravity is $\Delta L_z = z_c - \frac{h}{2}$, where the center of the water gravity is expressed by apparent position, z_a, $z_c = \frac{h}{2} + \frac{{z_a}^2}{6h}$. Combining the $\tan\varphi = \frac{z_a}{R}$, thus, the Δh could be expressed as $\Delta h = \frac{R^2}{6h}(\tan\varphi)^2$. Furthermore, according the $\tan\varphi = \frac{a_\omega}{g} - \frac{\gamma\Delta\cos\theta}{2R\rho gh}$, which combines the influence of the inertia and the wettability, the relationship between the change of water position Δh, centrifugal acceleration a_ω, height of static water surface h, and contact angle hysteresis $\Delta\cos\theta$ can be expressed as $\Delta h = \frac{R^2 a_\omega}{6g^2 h}\left(a_\omega - \frac{\gamma\Delta\cos\theta}{R\rho h}\right)$.

Supplementary Materials

The PDF file includes:

Figs. S1 to S27
Table S1
Legends for movies S1 to S3

Other Supplementary Material for this manuscript includes the following:

Movies S1 to S3

REFERENCES AND NOTES

1. W. B. DeOreo, P. Mayer, B. Dziegielewski, J. Kiefer, *Residential End Uses of Water, Version 2: Executive Report* (Water Research Foundation, 2016).
2. C. Duez, C. Ybert, C. Clanet, L. Bocquet, Wetting controls separation of inertial flows from solid surfaces. *Phys. Rev. Lett.* **104**, 084503 (2010).
3. S. Babaee, S. Pajovic, A. Rafsanjani, Y. Shi, K. Bertoldi, G. Traverso, Bioinspired kirigami metasurfaces as assistive shoe grips. *Nat. Biomed. Eng.* **4**, 778–786 (2020).
4. W. Poewe, K. Seppi, C. M. Tanner, G. M. Halliday, P. Brundin, J. Volkmann, A. Schrag, A. E. Lang, Parkinson disease. *Nat. Rev. Dis. Primers* **3**, 17013 (2017).
5. R. B. Bloem, S. M. Okun, C. Klein, Parkinson's disease. *Lancet* **397**, 2284–2303 (2021).
6. S. Sun, G. Wu, Sloshing in a tank with elastic side walls and a membrane cover. *Phys. Fluids* **36**, 102127 (2024).
7. H. C. Mayer, R. Krechetnikov, Walking with coffee: Why does it spill? *Phys. Rev. E* **85**, 046117 (2012).
8. C. Troll, J. P. Majschak, Modeling transient liquid slosh behavior at variable operating speeds induced by intermittent motions in packaging machines. *Appl. Sci. Basel* **10**, 1859 (2020).
9. A. Sauret, F. Boulogne, J. Cappello, E. Dressaire, H. A. Stone, Damping of liquid sloshing by foams. *Phys. Fluids* **27**, 022103 (2015).
10. X. Jin, C. Dai, Y. Tao, J. Chen, M.-M. Liu, C. Zhang, Effects of seismic characteristics and baffle damping on liquid sloshing. *Phys. Fluids* **36**, 013613 (2024).
11. J. Han, A study on the coffee spilling phenomena in the low impulse regime. *Achiev. Life Sci.* **10**, 87–101 (2016).
12. A. M. Worthington, R. S. Cole, Impact with a liquid surface studied by the aid of instantaneous photography II. *Philos. Trans. R. Soc. Lond. A* **194**, 175–199 (1900).
13. Y. Chen, Z. Liu, Z. Wang, Y. Yi, C. Yan, W. Xu, F. Zhou, Y. Gao, Q. Zhou, C. Zhang, H. Deng, Bioinspired robust gas-permeable on-skin electronics: Armor-designed nanoporous flash graphene assembly enhancing mechanical resilience. *Adv. Sci.* **11**, 2402759 (2024).
14. N. Song, Y. Yu, Y. Zhang, Z. Wang, Z. Guo, J. Zhang, C. Zhang, M. Liang, Bioinspired hierarchical self-assembled nanozyme for efficient antibacterial treatment. *Adv. Mater.* **36**, 2210455 (2023).
15. Z. Wang, H. Hu, Z. Chai, Y. Hu, S. Wang, C. Zhang, C. Yan, J. Wang, W. Coll, T. J. Huang, X. Xu, H. Deng, Bioinspired hydrophobic pseudo-hydrogel for programmable shape-morphing. *Nat. Commun.* **16**, 875 (2025).
16. X. Cheng, Z. Shen, Y. Zhang, Bioinspired 3D flexible devices and functional systems. *Natl. Sci. Rev.* **11**, nwad314 (2024).
17. A. Pringle, S. N. Patek, M. Fischer, J. Stolze, N. P. Money, The captured launch of a ballistospore. *Mycologia* **97**, 866–871 (2005).
18. R. Mukherjee, H. A. Gruszewski, L. T. Bilyeu, D. G. Schmale, J. B. Boreyko, Synergistic dispersal of plant pathogen spores by jumping-droplet condensation and wind. *Proc. Natl. Acad. Sci. U.S.A.* **118**, e2106938118 (2021).
19. A. R. Parker, C. R. Lawrence, Water capture by a desert beetle. *Nature* **414**, 33–34 (2001).
20. Y. Zheng, H. Bai, Z. Huang, X. Tian, F. Nie, Y. Zhao, J. Zhai, L. Jiang, Directional water collection on wetted spider silk. *Nature* **463**, 640–643 (2010).
21. T. Eisner, D. J. Aneshansley, Spray aiming in bombardier beetles: Jet deflection by the Coanda effect. *Science* **215**, 83–85 (1982).
22. T.-S. Wong, S. H. Kang, S. K. Y. Tang, E. J. Smythe, B. D. Hatton, A. Grinthal, J. Aizenberg, Bioinspired self-repairing slippery surfaces with pressure-stable omniphobicity. *Nature* **477**, 443–447 (2011).
23. H. Chen, P. Zhang, L. Zhang, H. Liu, Y. Jiang, D. Zhang, Z. Han, L. Jiang, Continuous directional water transport on the peristome surface of *Nepenthes alata*. *Nature* **532**, 85–89 (2016).
24. F. Chen, Z. Cheng, C. Gao, C. Li, C. Zhang, C. Yu, Z. Dong, L. Jiang, Capillarity constructed open siphon for sustainable drainage. *Small* **20**, 2307079 (2024).
25. C. Gao, Z. Liu, T. Shen, Z. Cheng, F. Chen, S. Liu, L. Jiang, Z. Dong, Water lily-inspired notch for passive stabilization in floating devices. *Device* **2**, 100405 (2024).
26. L. Yang, W. Li, J. Lian, H. Zhu, Q. Deng, Y. Zhang, J. Li, X. Yin, L. Wang, Selective directional liquid transport on shoot surfaces of *Crassula muscosa*. *Science* **384**, 1344–1349 (2024).
27. J. Wei, A. Rico-Guevara, S. W. Nicolson, F. Brau, P. Damman, S. N. Gorb, Z. Wu, J. Wu, Honey bees switch mechanisms to drink deep nectar efficiently. *Proc. Natl. Acad. Sci. U.S.A.* **120**, e2305436120 (2023).
28. E. J. Challita, M. S. Bhamla, Unifying fluidic excretion across life from cicadas to elephants. *Proc. Natl. Acad. Sci. U.S.A.* **121**, e2317878121 (2024).
29. G. Chomicki, G. Burin, L. Busta, J. Gozdzik, R. Jetter, B. Mortimer, U. Bauer, Convergence in carnivorous pitcher plants reveals a mechanism for composite trait evolution. *Science* **383**, 108–113 (2024).
30. W. Adlassnig, M. Peroutka, T. Lendl, Traps of carnivorous pitcher plants as a habitat: Composition of the fluid, biodiversity and mutualistic activities. *Ann. Bot.* **107**, 181–194 (2011).
31. H. F. Bohn, W. Federle, Insect aquaplaning: *Nepenthes* pitcher plants capture prey with the peristome, a fully wettable water-lubricated anisotropic surface. *Proc. Natl. Acad. Sci. U.S.A.* **101**, 14138–14143 (2004).
32. N. Gao, F. Geyer, D. W. Pilat, S. Wooh, D. Vollmer, H. Butt, R. Berger, How drops start sliding over solid surfaces. *Nat. Phys.* **14**, 191–196 (2017).
33. R. Ledesma-Aguilar, R. Nistal, A. Hernández-Machado, I. Pagonabarraga, Controlled drop emission by wetting properties in driven liquid filaments. *Nat. Mater.* **10**, 367–371 (2011).

34. U. Bauer, M. Paulin, D. Robert, G. P. Sutton, Mechanism for rapid passive-dynamic prey capture in a pitcher plant. *Proc. Natl. Acad. Sci. U.S.A.* **112**, 13384–13389 (2015).
35. D. E. Moulton, H. Oliveri, A. Goriely, C. J. Thorogood, Mechanics reveals the role of peristome geometry in prey capture in carnivorous pitcher plants (*Nepenthes*). *Proc. Natl. Acad. Sci. U.S.A.* **120**, e2306268120 (2023).
36. C. Li, C. Yu, S. Zhou, Z. Dong, L. Jiang, Liquid harvesting and transport on multiscaled curvatures. *Proc. Natl. Acad. Sci. U.S.A.* **117**, 23436–23442 (2020).
37. Xiaomi SU7 Ultra (Xiaomi Automobile Co. Ltd, 2024); www.xiaomiev.com/ultra.
38. CR400BF (China-EMU, 2024); www.china-emu.cn/Trains/Model/Detail-13050-105-39.html.
39. C919 aircraft (COMAC, 2024); www.comac.cc/cpyzr/c919/.
40. R. Tadmor, P. Bahadur, A. Leh, H. E. N'guessan, R. Jaini, L. Dang, Measurement of lateral adhesion forces at the interface between a liquid drop and a substrate. *Phys. Rev. Lett.* **103**, 266101 (2009).
41. L. Gao, T. J. McCarthy, Contact angle hysteresis explained. *Langmuir* **22**, 6234–6237 (2006).
42. C. Duez, C. Ybert, C. Clanet, L. Bocquet, Making a splash with water repellency. *Nat. Phys.* **3**, 180–183 (2007).
43. R. A. Ibrahim, *Liquid Sloshing Dynamics: Theory and Applications* (Cambridge Univ. Press, 2009).
44. B. Apffel, F. Novkoski, A. Eddi, E. Fort, Floating under a levitating liquid. *Nature* **585**, 48–52 (2020).
45. R. Adkins, I. Kolvin, Z. You, S. Witthaus, M. C. Marchetti, Z. Dogic, Dynamics of active liquid interfaces. *Science* **377**, 768–772 (2022).
46. P. Sartori, D. Quagliati, S. Varagnolo, M. Pierno, G. Mistura, F. Magaletti, C. M. Casciola, Drop motion induced by vertical vibrations. *New J. Phys.* **17**, 113017 (2015).

Acknowledgments: We thank the Shanghai Synchrotron Radiation Facility of BL13HB (https://cstr.cn/31124.02.SSRF.BL13HB) for the assistance on in situ synchrotron x-ray microtomography, in particular, Y. Xue and J. Fang for the technical support in the beamline BL13HB. We thank Z. Wei from the South China Botanical Garden, Chinese Academy of Sciences, for providing technical support in the phylogenetic analysis. We thank X. Xie from the Xishuangbanna Tropical Botanical Garden, Chinese Academy of Sciences, as well as X. Xie's guide, for investigating the pitcher plant samples and for imaging and analyzing the pitcher plants during the field investigation in Indonesia. We thank Prof. R. Li, Prof. F. Wu, and Prof. M. Liu from the Xishuangbanna Tropical Botanical Garden, Chinese Academy of Sciences (XTBG) for providing technical support and technical guidance. **Funding:** We acknowledge project funding provided by the National Natural Science Foundation (52173293 and 22122508 to Z.D. and 22205245 to C.Y.), the National Key Research and Development Program of China (2021YFA0716702 to C.Y.), and the Young Elite Scientists Sponsorship Program by China Association for Science and Technology (Z.D.). **Author contributions:** Conceptualization: Z.D. and L.J. Methodology: C.Y., L.W., and Z.D. Investigation: J.M., Z.Zhang, Z.Zhan, J.P., C.Y., L.W., and Z.D. Visualization: J.M., Z.Zhang, Z.L., C.Y., L.W., and Z.D. Supervision: C.Y., L.J., L.W., and Z.D. Writing—original draft: J.M. and Z.D. Writing—review and editing: C.Y., L.J., L.W., and Z.D. **Competing interests:** The dual-biomimetic cup for anti-sloshing is covered by two pending CNIPA patents: CN2025112564997 (2025.09.04) and CN2025112782402 (2025.09.09). Applicants: Beijing Institute of Future Science and Technology on Bioinspired Interface. Inventors Jie Ma, Cunlong Yu, Zhichao Dong, and Lei Jiang are also paper authors. All other authors declare no competing interests. **Data and materials availability:** All data needed to evaluate the conclusions in the paper are present in the paper and/or the Supplementary Materials.

Submitted 11 June 2025
Accepted 15 October 2025
Published 14 November 2025
10.1126/sciadv.adz7099

Science Advances

Bioinspired wettability boundary stabilizes water sloshing

Jie Ma, Zidong Zhan, Zihao Zhang, Zhuoxing Liu, Jia Peng, Cunlong Yu, Lei Jiang, Lei Wu, and Zhichao Dong

Sci. Adv. **11** (46), eadz7099. DOI: 10.1126/sciadv.adz7099

Science Advances (ISSN 2375-2548) is published by the American Association for the Advancement of Science. 1200 New York Avenue NW, Washington, DC 20005. The title *Science Advances* is a registered trademark of AAAS.